CrossMark

Design and development of a high resolution animal SPECT scanner dedicated for rat and mouse imaging

Salar Sajedi [a], Navid Zeraatkar [a], Vahideh Moji [a,b], Mohammad Hossein Farahani [a,b], Saeed Sarkar [a,c], Hossein Arabi [a], Behnoosh Teymoorian [a,b], Pardis Ghafarian [d,e], Arman Rahmim [f,g], Mohammad Reza Ay [a,c,*]

[a] Research Center for Molecular and Cellular Imaging, Tehran University of Medical Sciences, Tehran, Iran
[b] Parto Negar Persia Co, Tehran, Iran
[c] Department of Medical Physics and Biomedical Engineering, Tehran University of Medical Sciences, Tehran, Iran
[d] Chronic Respiratory Disease Research Center, NRITLD, Masih Daneshvari Hospital, Shahid Beheshti University of Medical Sciences, Tehran, Iran
[e] PET/CT and Cyclotron Center, Masih Daneshvari Hospital, Shahid Beheshti University of Medical Sciences, Tehran, Iran
[f] Department of Radiology, Johns Hopkins University, Baltimore, MD, USA
[g] Department of Electrical and Computer Engineering, Johns Hopkins University, Baltimore, MD, USA

ARTICLE INFO

ABSTRACT

A dedicated small-animal SPECT system, HiReSPECT, was designed and developed to provide a high resolution molecular imaging modality in response to growing research demands. HiReSPECT is a dual-head system mounted on a rotating gantry. The detection system is based on pixelated CsI(Na) scintillator crystals coupled to two Hamamatsu H8500 Position Sensitive Photomultiplier Tubes in each head. Also, a high resolution parallel-hole collimator is applied to every head. The dimensions of each head are 50 mm × 100 mm, enabling sufficient transaxial and axial fields-of-view (TFOV and AFOV), respectively, for coverage of the entire mouse in single-bed position imaging. However, a 50 mm TFOV is not sufficient for transaxial coverage of rats. To address this, each head can be rotated by 90 degrees in order to align the larger dimension of the heads with the short body axis, allowing tomographic data acquisition for rats. An innovative non-linear recursive filter was used for signal processing/detection. Resolution recovery was also embedded in the modified Maximum-Likelihood Expectation Maximization (MLEM) image reconstruction code to compensate for Collimator-Detector Response (CDR). Moreover, an innovative interpolation algorithm was developed to speed up the reconstruction code. The planar spatial resolution at the head surface and the image spatial resolutions were 1.7 mm and 1.2–1.6 mm, respectively. The measurements followed by post-processing showed that the observed count rate at 20% count loss is about 42 kcps. The system sensitivity at the collimator surface for heads 1 and 2 were 1.32 cps/μCi and 1.25 cps/μCi, respectively. The corresponding values were 1.18 cps/μCi and 1.02 cps/μCi at 8 cm distance from the collimator surfaces. In addition, whole-body scans of mice demonstrated appropriate imaging capability of the HiReSPECT.

1. Introduction

Single photon emission computed tomography (SPECT) is a technology for functional medical imaging with an increasing importance in both medical diagnosis and monitoring response to therapy [1,2]. During the recent years, the use of small animal models in in-vivo biomedical research has been growing. This has resulted in an emerging need for dedicated small animal imaging systems that provide better spatial resolution and sensitivity [3–9].

In this way, there are significant advancements happening both on the instrumentation front for data acquisition and in the development of reconstruction methods for extracting images from the acquired data.

Most small animal SPECT systems have been developed based on pinhole or multi-pinhole collimation technique as reported in the literature [10–15]. Few dedicated small animal systems have been designed and developed based on parallel-hole collimation system. YAP-(S)PET scanner is a hybrid PET/SPECT system whose SPECT modality consists of two heads. Each head is based on an array of 400 Yttrium Aluminum Perovskit-Ce Activated (YAP:Ce) finger crystals with size of 2 mm × 2 mm × 30 mm coupled to Hamamatsu R2486 position sensitive photomultiplier tubes (PSPMTs). Both transaxial and axial field of view (FOV) of the system is 4 cm

* Corresponding author at: Tehran University of Medical Sciences, Department of Medical Physics and Biomedical Engineering, Pousina St, Tehran, Iran.
Tel./fax: +98 21 66907532.
E-mail address: mohammadreza_ay@sina.tums.ac.ir (M. Reza Ay).

providing a spatial resolution below 2 mm and a sensitivity of 640 cps/μCi at the center [16,17]. Choong et al. [18] designed a small animal SPECT for imaging of I-125 low energy radioisotope using pixelated lithium-drifted silicon (Si(Li)) detectors. The system has 2 heads; each head consists of 64×40 crystal pixels with the size of $1 \text{ mm} \times 1 \text{ mm} \times 30 \text{ mm}$. The expected spatial resolution and sensitivity for the system is about 1.6 mm and 6.7 cps/μCi, respectively. Loudos et al. [3,19] developed a small animal gamma camera using R2486 PSPMT and a 4 mm thick round pixelated Cesium Iodide-Thallium Activated (CsI(Tl)) crystal. The size of each pixel is 1.13 mm². The planar and tomographic spatial resolution of the system is 2 mm and 2–3 mm, respectively. Weisenberger et al. [20] developed a dual head system for restraint free small animal SPECT imaging. The Sodium Iodide-Thallium Activated (NaI(Tl)) pixelated crystal coupled to Hamamatsu R8520-C12 PSPMTs formed the detection system. The pixel size is $2 \text{ mm} \times 2 \text{ mm} \times 15 \text{ mm}$. Linoview system is based on direct acquisition of linogram projections using slit-aperture collimators. The system has 4 heads; each head consists of a pixelated Cesium Iodide-Sodium Activated (CsI(Na)) crystal with pixel size of $2.5 \text{ mm} \times 2.5 \text{ mm} \times 5 \text{ mm}$ coupled to Hamamatsu R8520-00-C12 PSPMTs. Phantom studies showed that Linoview can distinguish hot rods separated by 0.35 mm [21]. Loudos et al. [22–24] developed a mouse-sized gamma camera using pixelated NaI(Tl) crystal and Hamamatsu H8500 PSPMTs. The size of crystal pixels is $1 \text{ mm} \times 1 \text{ mm} \times 5 \text{ mm}$. The planar spatial resolution reported ~ 1.6 mm on the collimator surface and increasing to ~ 4.1 mm at 12 cm distance from the collimator. In addition, the average energy resolution was measured 15.6% for Tc-99m. In another design, Hamamatsu C9177 radiation imager module has been mounted on a rotary gantry to form a SPECT system [25]. The module consists of pixelated CsI(NaI) crystal with pixel size of $1.9 \text{ mm} \times 1.9 \text{ mm} \times 6 \text{ mm}$ coupled to Hamamatsu R8400-M64 PSPMT. Energy resolution reported 11.6% and sensitivity and planar spatial resolution on the surface was 2.54 cps/μCi and 2.4 mm, respectively. Villena et al. [26] employed a super resolution technique to enhance the spatial resolution in their SPECT system. The detection system consists of pixelated NaI(Tl) crystal with pixel size of $1.4 \text{ mm} \times 1.4 \text{ mm} \times 6 \text{ mm}$ coupled to Hamamatsu H8500 PSPMTs. They reached a planar spatial resolution of ~ 1.6 mm and tomographic spatial resolution below 4 mm.

In this study, we report our preliminary results and design concept of the high resolution SPECT (HiReSPECT) for small animal imaging. The system was extensively evaluated and tested utilizing phantoms as well as live animals. The aim was to develop a system with high resolution, appropriate sensitivity, and flexibility to image both mouse and rat models.

2. Materials and methods

2.1. Detection system

We utilized a dual head configuration with 180 degrees angular distance for the detection subsystem of the HiReSPECT. In each head, two H8500C flat panel PSPMTs (Hamamatsu Photonics Co., Japan) were tightly attached to one another to form an active detection area of about $100 \text{ mm} \times 50 \text{ mm}$. Each H8500C PSPMT includes 8×8 pixel with separate anode signals and physical pitch size of 6.08 mm at PSPMT surface.

Each pair of H8500C PSPMTs was fixed to a pixelated CsI(Na) crystal using optical grease. The crystal consists of an array of 80×38 pixel. The size of each pixel is $1 \text{ mm} \times 1 \text{ mm} \times 5 \text{ mm}$, and the size of epoxy septum between the pixels is 0.2 mm leading to a pitch size of 1.2 mm. The active area of the crystal is about $100 \text{ mm} \times 50 \text{ mm}$. There is a 50 μm-thick aluminum entrance window and also a 3 mm-thick glass window at the two sides of the crystal facing the gamma rays and the PSPMTs, respectively.

A high resolution parallel-hole collimator (Nuclear Fields Co., Australia) was utilized for each head. The face-to-face distance, septa size, and thickness of the holes are 1.2 mm, 0.2 mm, and 34 mm, respectively. The active collimating area of the collimators is $108 \text{ mm} \times 56 \text{ mm}$.

All components of the detection system including the crystal, the PSPMTs, the preamplifier, the read-out electronics, and the high voltage (HV) boards were placed in aluminum housing shielded by at least 2 mm lead. The collimator is mounted on the frontal side of the housing.

2.2. Electronic readout and signal processing

A compact HV generator board was used to bias the H8500C PSMPTs. The operational HV was set to -900 V. Each H8500C pair produces 16×8 anode signals $(2 \times 8 \times 8)$. After pre-amplification of the signals, a voltage clamping technique was used to suppress weak signals diminishing final positioning accuracy. Then, we used a simple resistive network for generating position signals: X^+, X^-, Y^+, and Y^- to be used for Anger logic positioning (for more information see [27]).

In the acquisition board, four analog-to-digital converters (ADCs) were applied to digitize the position signals (i.e. X^+, X^-, Y^+, and Y^-). In order to have more precise digital conversion, thus better positioning, 16 bit-resolution ADCs were used. Although the ADCs have 16 bit resolution, only the 14 most significant bits (MSBs) are considered for processing. Conversion time of the ADCs is 0.3 μs. Additionally, for signal processing and detection, we used a method utilizing a novel non-linear recursive filter (NLRF) which we have previously developed [28]. The NLRF used in the acquisition board acquires two successive samples from the captured, amplified and shaped PMT signal. Sampling rate is fixed and is much lower than the sampling rates utilized in the conventional digital acquisition boards (3 MHz instead of minimum 20 MHz conventional rates). The two samples are used for indexing a look-up table in which previously-calculated maximum pulse amplitude for different sample pairs has been stored. In the same way, next samples will be predicted by different look-up tables. The prediction of consecutive samples will suppress detected pulse tale effect over next pulses (pile-up of two or more pulses). Eventually, via a USB port, the digital position signals are transferred to an in-house computer to be stored as List Mode Format (LMF) data.

All software, code, and graphical user interfaces (GUIs) are run on a computer with a Core i5 3.0 GHz CPU, 4 GB RAM memory, and 4 GB graphic card. The display consists of 2 wide LED monitors, one for acquisition and reconstruction and the other for 3 dimensional (3D) rendering and processing. In addition, one touch screen on an arm attached to the gantry has the same function as the first display monitor to ease the control and acquisition procedure for the user close to the system.

2.3. Gantry

The Gantry of the HiReSPECT, which is illustrated in Fig. 1, was designed and fabricated to be capable of installing 4 heads. Alternatively, 2 heads and an X-ray tube together with X-ray detectors can be set up in order to develop a SPECT/CT system. However, in the current version, only 2 opposing heads were installed to form a dual-head SPECT system configuration.

In addition to the heads, high accuracy gear boxes and stepper motors of the heads, data acquisition boards, switching power supplies, and a video camera were installed on the gantry. The video camera was utilized to view and monitor the animal inside
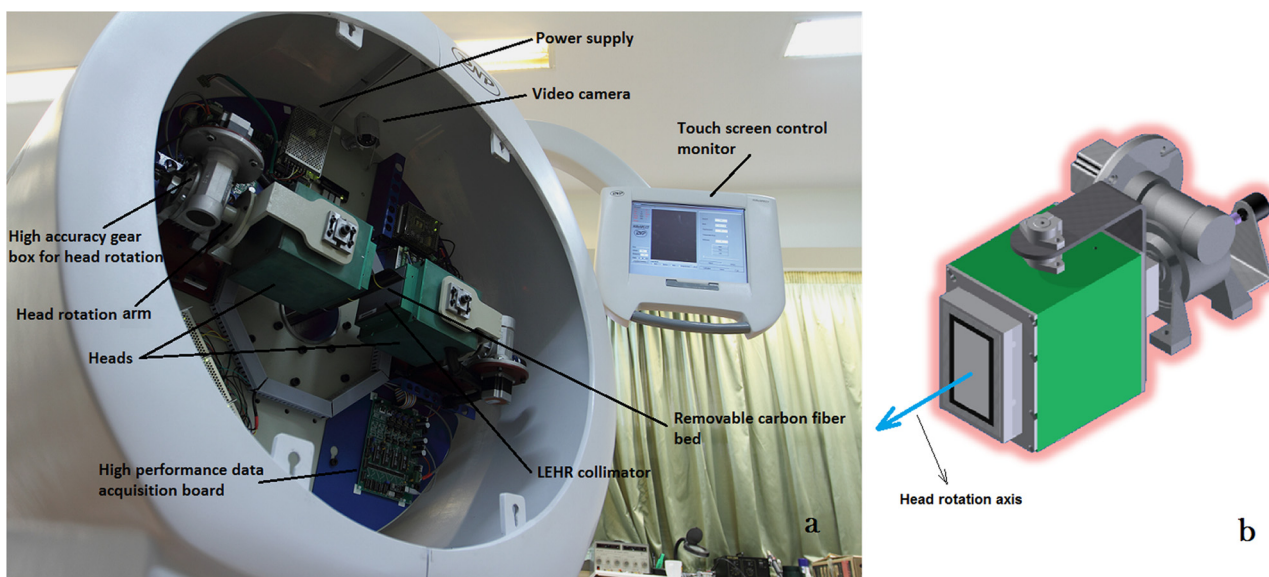
Fig. 1. The gantry of the HiReSPECT indicating its main parts (a), and the graphical illustration of one of the heads in rat mode (b).

the gantry during the scan, which also had an infra-red imaging capability suitable for dark conditions.

The heads can get closer to or farther from the center of rotation in order to alter the radius of rotation (ROR). Furthermore, through an innovative design, every head can rotate 90 degrees in order to align the larger dimension of the heads with the short body axis of the rat models. The rotation arm of the head is illustrated in Fig. 1a and the rotation axis is drawn in Fig. 1b. This way, the system is able to perform tomographic data acquisition for rat models with ~10 cm Transaxial FOV (TFOV) and about 5 cm Axial FOV (AFOV). This enables transaxial coverage of the rats, but imposes bed movements if whole-body axial coverage is desired. By contrast, for mouse imaging, the heads′ configuration provides ~5 cm TFOV and ~10 cm AFOV which enables the system to perform the mouse scan utilizing a single bed position. While the heads in Fig. 1a are set in mouse mode, Fig. 1b shows one of the heads in rat mode.

The entire gantry can rotate clockwise and counter-clockwise from 0 degrees to 370 degrees with a precision of 0.14 degrees through step-and-shoot or continuous acquisition modes.

The bed was constructed from carbon fiber to be strong enough from one side and also as transparent as possible to gamma rays from the other side. The bed can move in and out for appropriate positioning of the animal in the FOV.

2.4. Calibrations

2.4.1. Linearity calibration
Linearity calibration and position mapping is the first and the most significant calibration for the HiReSPECT. A dedicated bar phantom as shown in Fig. 2a was developed to be used for position mapping and linearity calibration. Tungsten bars were applied to provide good attenuation. Every two neighboring bars are separated by a 0.2 mm gap (equal to pixel septa size). The width and the thickness of the bars are 4.8 mm (for times the pixel pitch size) and 5 mm, respectively.

The procedure of data acquisition for linearity calibration should be performed independently for every direction (X and Y) of the head. For each direction, two data acquisitions were performed. For data acquisition, a flood field Tc-99m source was placed on the bar phantom. First, the bars were adjusted so that the gaps were centered on the rows (columns). As shown in Fig. 2a, a caliper with 10 μm precision is mounted on the bar

phantom enabling it to precisely slide on the head and change the relative position of the bars. By several experiments, we found out when the gaps were with acceptable precision on the centers of the pixels: if the gaps were not matched with the pixels centers (but also were on the septa), 2 lines were seen in the image. With fine displacement of the bars, gradually these line pairs were merged and generated one hot line in the image. We considered this place as where the gaps are on the pixels centers. Then, data acquisition continued until at least 30 million counts were acquired. Afterwards, the bars were shifted 2.4 mm, and the same data acquisition process was performed. By merging the two planar images, which were acquired in 512×1024 matrices, a new matrix was generated showing the mapped position of a set of line sources with 2.4 mm distance. The position of the row (or column) between this 2.4 mm-distant lines (crystal pixel pitch is 1.2 mm), was obtained by linear interpolation. By repeating the same procedure for the other direction of the head, crossing points of the 2 sets of line source images showed the center of pixels. Regarding the information achieved, a lookup table (LUT) was generated to map every event position to its corrected position in a 40×80 matrix. This protocol should be repeated for each head independently.

Fig. 2b and c show the image of the linearity bar phantom in two directions respectively before and after linearity calibration in head 1.

2.4.2. Energy calibration
After linearity calibration, data were arranged in a 40×80 matrix. Then, energy calibration was performed using the Kohenen neural network [29] (for more information about the model, refer to classic Refs. [30,31]). For data acquisition, a flood field Tc-99m source was used on the detector in intrinsic mode (collimator removed).

2.4.3. Uniformity calibration
The same flood field source as the one used for energy calibration was applied in the same way for data acquisition. Then, a uniformity correction map was generated using the acquired data to correct for nonuniformity of the detector. Fig. 3 demonstrates the flood field image before and after uniformity calibration in both heads.
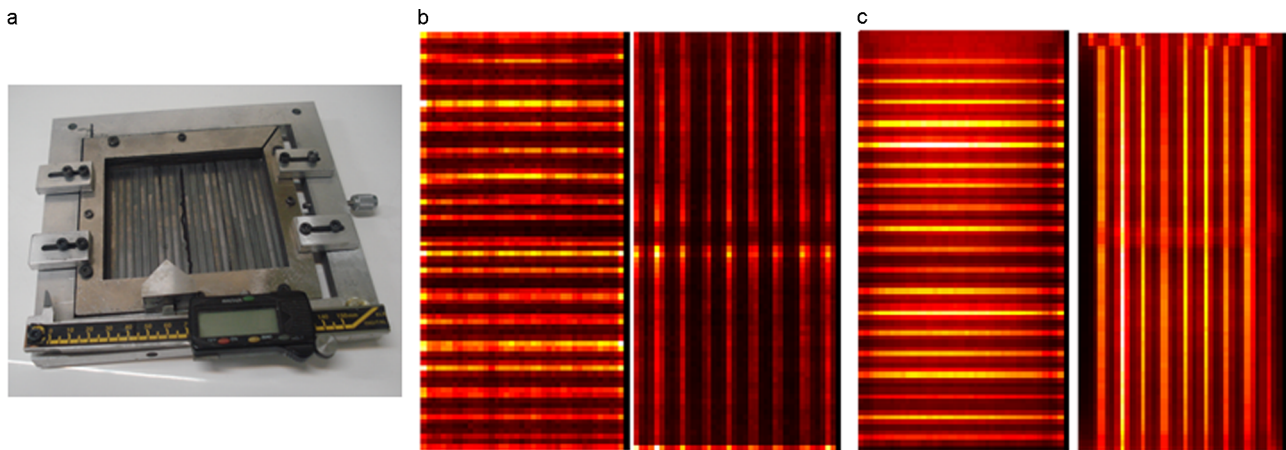
Fig. 2. The dedicated bar phantom developed for linearity calibration (a), the images of linearity bar phantom before (b) and after (c) linearity calibration in head 1.
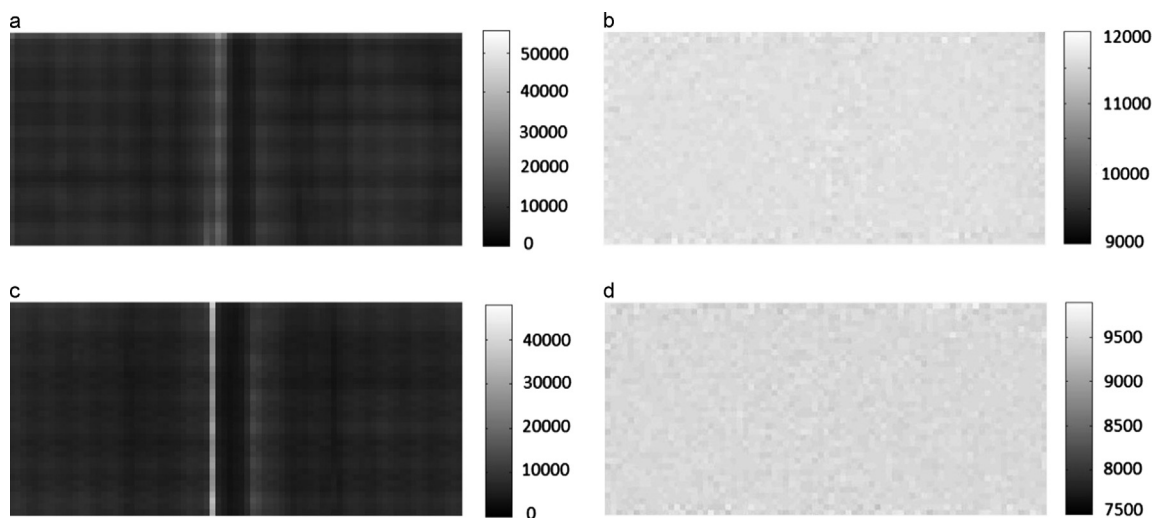

Fig. 3. Flood field image before (a) and after uniformity calibration (b) in head 1, and similarly in head 2 (c) and (d).

2.5. Image reconstruction

The data acquired in each view are stored in a 38×80 matrix called projection matrix. However, a 3D $128 \times 128 \times 240$ matrix is considered for image reconstruction. The default mode for SPECT data acquisition is 30 views in 180 degrees per head (thus 360 degrees for both heads). The images are then reconstructed using the 3D Maximum-Likelihood Expectation Maximization (MLEM) algorithm [32]. This included implementation of a rotation-based algorithm to speed up the final reconstruction code [33,34]. To speed up reconstructions, we performed analytic matrix rotation calculations offline and created look-up tables (LUTs). In particular, we used 78-degree rotations to reduce the size of the LUTs. This is because it turns out that at this angle, only 5 target pixels are needed for interpolation of each source pixel, as opposed to the standard 9 target pixels in the classical implementation of bilinear rotation. A full iteration starts from the first view and continues successively by 78-degree rotations, enabling 180-degree tomographic coverage with 6 degree increments after 29 rotations. This results in 30 total views as considered by the MLEM sub-iterations, though in a different order than conventional monotonically increasing angular coverage. As SPECT imaging is challenged by the presence of resolution degrading phenomena [35], leading to the Collimator-Detector Response (CDR) [36], CDR modeling (resolution recovery) was also embedded in the reconstruction code. For this, the CDR function (CDRF) corresponding to three different distances from the collimator was characterized empirically using measured point sources and subsequent fits using 2D Gaussian functions. The code generates the CDRF corresponding to every distance from the collimator using the measured CDRFs and interpolating each of the 2D Gaussian widths for the remaining distances from the head. For compensating the CDRF, every plane parallel to the head in the image matrix is convolved by the corresponding CDRF before forward projection and after back projection during the reconstruction.

2.6. Assessment of system performance

2.6.1. Energy resolution

A point source of Tc-99m was placed at 35 cm distance from the detector without collimator and data acquisition was performed while storing the energy of every event. The average energy spectrum was then obtained using all pixels of the crystal and its FWHM divided by the peak energy (140.5 keV) expressed as the energy resolution of the detector.

2.6.2. Spatial resolution

For assessing the planar spatial resolution of the system, the method applied by Loudos et al. [22] was utilized. A capillary with inner diameter of 1.1 mm Tc-99m solution was used. A combination of 5 capillary sources was scanned for judging the tomographic

spatial resolution of the system after image reconstruction. The distance between each two adjacent capillary is indicated in Fig. 4a. Data were then reconstructed with and without resolution recovery using 2 full iterations.

Moreover, a Jaszczak phantom was developed to assess the spatial resolution of the reconstructed image of the system. As shown in Fig. 5a, the main part of the phantom is a cylinder with 35 mm height and 32 mm diameter. Inside it, various fillable rods were drilled in 6 sections. The radius of rods ranges from 1.8 mm to 2.8 mm with the steps of 2 mm from section to section. In each section, the distance between every 2 rods is equal to the radius of the rods in the section. The container of the phantom is a cylinder having a hollow for the main phantom part to be fitted in and a lid for packing the phantom. For data acquisition, the phantom was filled uniformly with Tc-99m dissolved in normal saline. The data were then reconstructed with and without resolution recovery.

2.6.3. Intrinsic count rate performance

We used the method suggested by Geldenhuys et al. [37] for assessment of the intrinsic count rate performance. In this way,
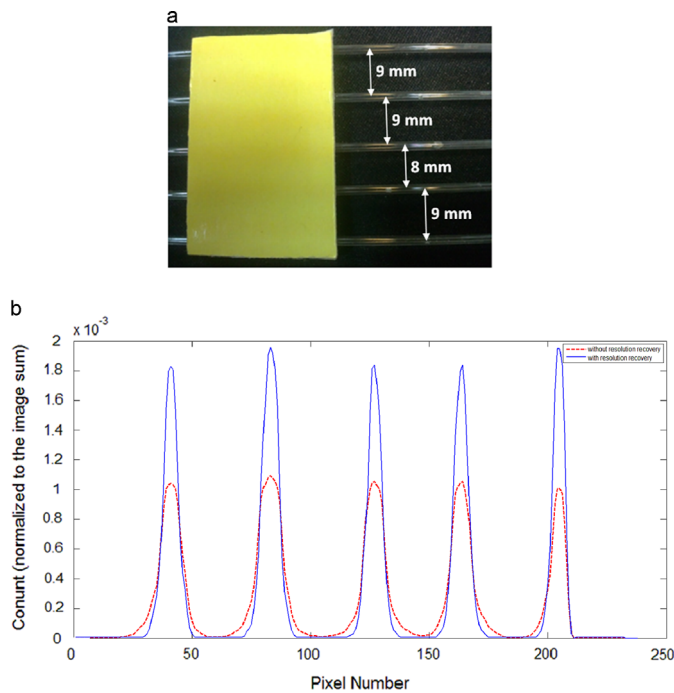
Fig. 4. The configuration of the 5 capillaries showing their relative distances (a), the count profiles passing the center of the rods in one slice of the reconstructed images of the 5 capillaries after 2 iterations without and with resolution recovery (b). The values in without-resolution–recovery and with-resolution–recovery count profiles are normalized to sum of images without resolution recovery and with resolution recovery, respectively.
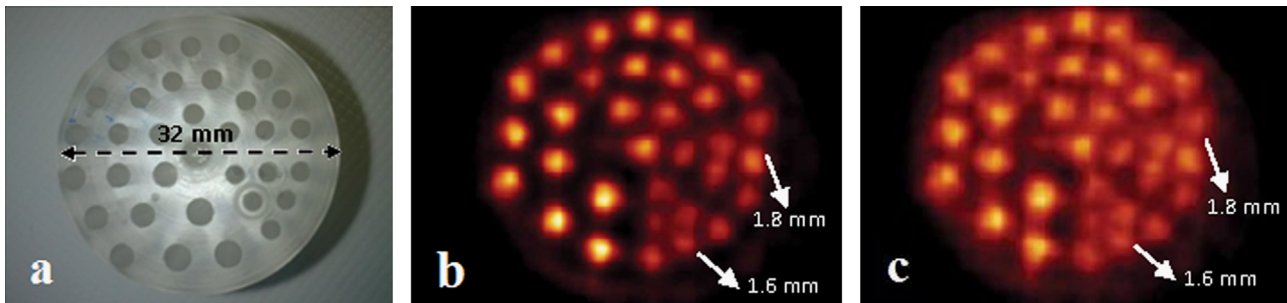
the incident photon flux was modulated by placing copper attenuator plates with thicknesses of 2 mm between the source and the head while the collimator was removed. A Tc-99m source with the activity of 5 mCi was placed 35 cm distant from the head. The number of copper plates increased for each experiment and the planar image was stored. The total number of the counts in each step was corrected for decay and divided by the acquisition time to form the observed count rate (OCR) of the step. By plotting the logarithm of OCR versus the thickness of the attenuator (copper plates) and fitting a line on the low count rate section of the data, the true count rate (TCR) versus the number of the attenuator plates was achieved. The OCR in which the TCR and OCR have 20% difference was measured and reported as the OCR at 20% count loss.

2.6.4. System sensitivity

In order to measure the system sensitivity, a cylindrical phantom with inner diameter of 32 mm and the height of 5 mm was filled with 2 mCi Tc-99m. The phantom was then placed at the distances of 0 cm and 8 cm from the collimator in a way that the circular cross-section was parallel to the head. Data acquisition was done for 300 s at each step. The total counts in each image was corrected for the decay and considered as the counts at the corresponding distance. The sensitivity was then calculated by dividing the corrected counts by the total time.

2.6.5. Animal study

Two mouse studies including Tc-99m-methylene diphosphonate (MDP) and Tc-99m-dimercapto succinic acid (DMSA) were performed for skeletal scan and renal scintigraphy, respectively. An activity of 2 mCi was injected to the mice in each study and data acquired using the default protocol of acquisition. Data acquisition time for each view was 60 s. The mice were placed under general anesthesia during the scans. Fig. 7a shows an anesthetized mouse lying on the scanner table prior to the start of the scan. The data were then reconstructed using the default reconstruction parameters.

3. Results

The averaged energy resolution at 140.5 keV was about 20% for both heads with negligible differences. Planar resolution measured using the mentioned method was 1.7 mm in terms of FWHM.

Fig. 4b shows the count profile passing the centers of the capillaries (illustrated in Fig. 4a) in a slice of the reconstructed images with and without resolution recovery. The data were normalized to the sum of the corresponding images in order to provide a better comparison. Fig. 4b shows the improvement in spatial resolution after applying resolution recovery leading to sharper peaks in the corresponding count profile. In addition, the spatial resolution was measured in terms of FWHM along radial and tangential directions. The results are summarized in Table 1

Fig. 5. The main part of the Jaszczak phantom developed for spatial resolution assessment (a) together with one slice of its reconstructed image after 2 iterations with resolution recovery (b) and without resolution recovery (c).

Table 1
Spatial resolution in different radial offsets with and without resolution recovery after 2 iterations.

Radial offset (mm)	Without resolution recovery		With resolution recovery	
	Radial FWHM (mm)	Tangential FWHM (mm)	Radial FWHM (mm)	Tangential FWHM (mm)
5.2	2.2	2.4	1.6	1.8
7.5	2.5	2.5	1.7	1.8
11.3	2.1	2.4	1.6	1.7
16.0	2.4	2.4	1.7	1.7
19.6	1.6	2.4	1.2	1.5
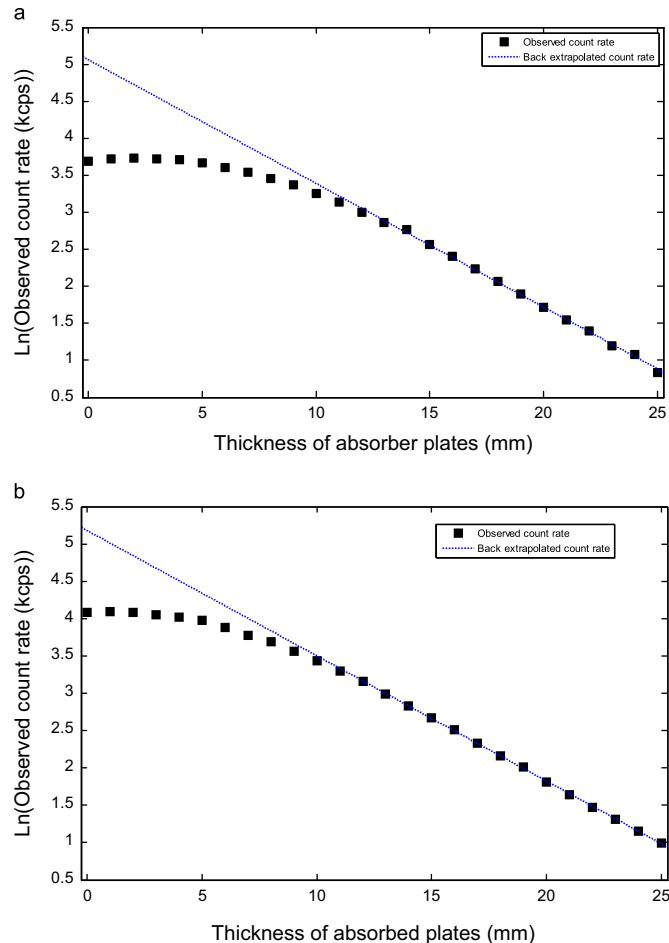
Fig. 6. The observed count rate (OCR) from a Tc-99m point source against the thickness of copper plates for head 1 (a) and head 2 (b). A line fitted on the low count rate section for determination of true count rate.

showing that the tangential and radial FWHM range respectively from 1.5 mm to 1.8 mm and 1.2 mm to 1.7 mm when the radial offset varies from approximately 20 mm to 5 mm.

Fig. 5b shows one transaxial slice of the reconstructed image of the Jaszczak phantom with resolution recovery. It can be seen that the image with resolution recovery is visually clear with adequate resolving in the sections containing 1.6 mm and 1.8 mm rods. In contrast, the mentioned sections are not appropriately resolved in Fig. 5c which is reconstructed without resolution recovery.

Fig. 6a and b depict the logarithm of OCR versus the thickness of the attenuator for head1 and head 2, respectively. A line was fitted on the linear region of the data. In addition, it was calculated that the OCR for 20% count loss is about 42 kcps for both heads. The system sensitivity at the collimator surface was 1.32 cps/μCi

and 1.25 cps/μCi for head 1 and head 2, respectively. This value is 1.18 cps/μCi and 1.02 cps/μCi at 8 cm distance for head 1 and head 2, respectively.

Fig. 7b shows the reconstructed image of the whole-body scans of a mouse with resolution recovery using MDP. Similarly, Fig. 7c depicts the reconstructed image of the whole-body scan with resolution recovery performed after administration of DMSA. The images illustrate the snapshots of 3D rendering in Maximum Intensity Projection (MIP) mode. No smoothing filter applied on projection data.

4. Discussion

Since one of our priorities for developing the HiReSPECT was a large coverage of mice and rats, we utilized parallel-hole collimators, in particular enabling single-bed whole-body imaging of mice. Furthermore, despite good spatial resolution of the pinhole collimator in small distances from the pinhole, its spatial resolution and sensitivity gets severely worse when the distance from the pinhole increases [38,39], though this can be addressed by appropriate distance and use of numerous pinholes surrounding the object [34], posing expense considerations.

Selection of the flat panel PSPMT should be performed taking into account the size of the pixelated crystals. As an example, Weisenberger et al. [20] showed that R8520 PSPMTs cannot resolve a crystal array with pixel sizes of 1 mm × 1 mm. However, they could resolve 2 mm × 2 mm pixel sizes by the same PSPMTs. Based on the literature [20,22–24,26], it can be concluded that for crystal pixel sizes of about 1 mm × 1 mm and in the case of parallel-hole collimation, the H8500 PSPMT is an appropriate option.

It should be noted that the NLRF algorithm is especially favorable for improving dead-time performance of detectors given its handling of very high count rates. Though such high count rates are not encountered in typical SPECT imaging, we used a simple and very low-cost hardware enabling this new signal processing approach.

After some pre-design Monte Carlo simulations, we selected the CsI(Na) crystal for use in the HiReSPECT. However, different kinds of scintillator crystals such as NaI(Tl) [20,22,23,25,26], YAP: Ce [17], CsI(Tl) [3,19] and CsI(NaI) [25] have been used in other small animal SPECT systems based on parallel-hole (or slit-hole) collimation. Even lithium-drifted silicon detectors (Si(Li)) were used in one system [18]. Most of the small animal SPECT systems, which used parallel hole collimator, applied NaI(Tl), CsI(Tl), or CsI (Na) scintillator crystals [3,19,20,22,23,25,26]. However, we chose CsI(Na) because according to our crystal provider (Hilger Crystals, England), the properties of these 3 crystal types are not so different while CsI(Na) was considerably low-cost.

The energy resolution of the HiReSPECT for Tc-99m is 21% which is poorer than what Loudos et al. reported in their works: 15.6% [22,24]. Though the pixel size of the crystal is the same in our work and theirs, this difference in energy resolution value may originate from using different crystal materials, namely CsI(Na) in the HiReSPECT vs. NaI(Tl) in theirs. The other reason can be the use of different front-end electronics, energy calibration method, etc.

Planar spatial resolution of the HiReSPECT at the collimator surface is 1.7 mm FWHM. Loudos et al. reported almost the same planar resolution (1.6 mm) using the same pixel size of the HiReSPECT [22,24], but reached 2 mm planar spatial resolution using 1.13 mm² crystal pixel sizes elsewhere [3,19]. This poorer spatial resolution may have resulted from the use of R2486 PSPMTs instead of H8500. Lage et al. [25] reported 2.4 mm planar resolution at the head surface using 1.9 mm × 1.9 mm pixel sizes and R8400-M64. This rather large spatial resolution is mainly due to the use of larger crystals in comparison to the HiReSPECT.
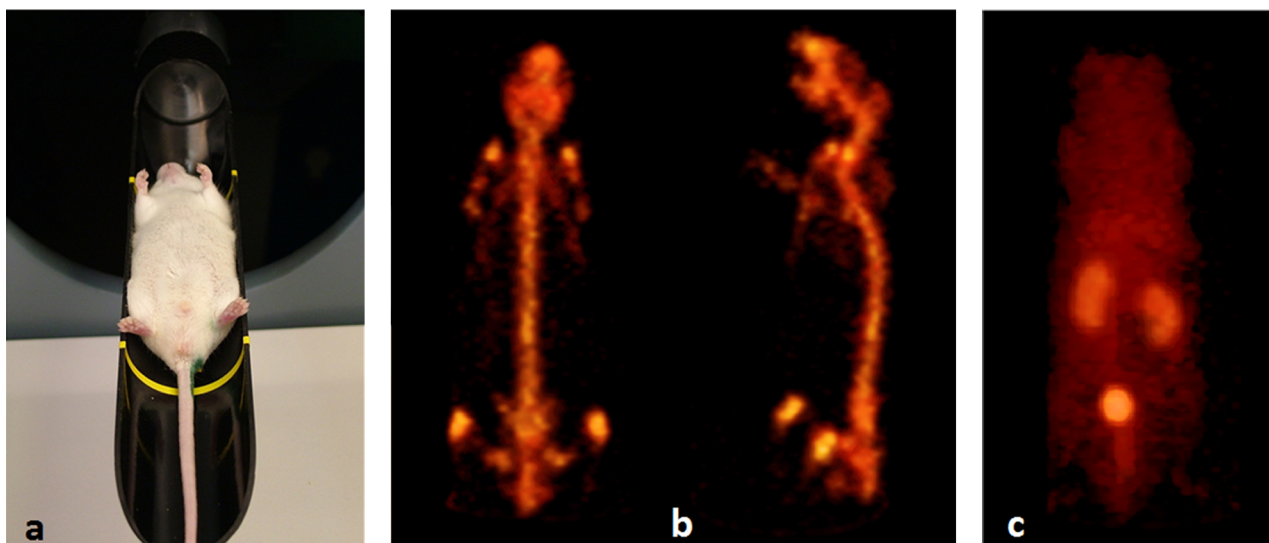
Fig. 7. An anesthetized injected mouse lies on the HiReSPECT bed prior to scan (a). Snapshots are shown of 3D renderings of the reconstructed images of mouse whole body scans (with resolution recovery) using tracers 99mTc-MDP (b) and 99mTc-DMSA (c).

The mouse whole-body images acquired by the HiReSPECT (Fig. 7b and c) reflect the good capability of the HiReSPECT in small animal imaging; skeletal structures as well as both kidneys together with the bladder of the mouse are clearly imaged.

One important novelty in the design of the HiReSPECT is the ability of its heads to rotate around their normal axis to provide a larger AFOV along their longer dimension. Using this flexibility, the HiReSPECT can easily change in-between the modes for the imaging of mice or rats.

We aim to enhance the image quality and also the quantitative accuracy by adding a CT module to the gantry to utilize CT-based attenuation correction. Also, we are working on the development of pinhole and multi-pinhole collimators for the current detectors to gain spatial resolution without compromising the sensitivity.

5. Conclusion

A dedicated small animal SPECT scanner was developed with high spatial resolution (1.7 mm in the planar mode and < 1.6 mm in the tomographic mode) and appropriate sensitivity (~ 1.3 cps/μCi). In addition, the observed count rate for 20% count loss is approximately 42 kcps. For signal processing/detection, a novel non-linear recursive filter was applied. Furthermore, a resolution–recovery-embedded MLEM code was utilized for image reconstruction. The system is capable of scanning rat and mouse models by changing its scan mode mechanically in an innovative mode. The whole body small animal scans showed appropriate imaging performance of the system.

References

[1] M.M. Khalil, J.L. Tremoleda, T.B. Bayomy, W. Gsell, Int. J. Med. Mol. Imaging 2011 (2011) 15.
[2] D.L. Bailey, K.P. Willowson, J. Nucl. Med. 54 (2013) 83.
[3] G.K. Loudos, K.S. Nikita, N.D. Giokaris, E. Styliaris, S.C. Archimandritis, A.D. Varvarigou, et al., Appl. Radiat. Isot. 58 (2003) 501.
[4] F.J. Beekman, B. Vastenhouw, Phys. Med. Biol. 49 (2004) 4579 (Oct).
[5] N. Kubo, S. Zhao, Y. Fujiki, A. Kinda, N. Motomura, C. Katoh, et al., Ann. Nucl. Med. 19 (2005) 633 (Oct).
[6] S.R. Meikle, F.J. Beekman, S.E. Rose, Drug Discovery Today: Technol. 3 (2006) 187.
[7] G. Loudos, S. Majewski, R. Wojcik, A. Weisenberger, N. Sakellios, K. Nikita, et al., IEEE Trans. Nucl. Sci. NS54 (2007) 454 (Jun).
[8] J.G. Qian, E.L. Bradley, S. Majewski, V. Popov, M.S. Saha, M.F. Smith, et al., Nucl. Instrum. Methods Phys. Res., Sect. A 594 (2008) 102 (Aug).
[9] G.S. Mitchell, S.R. Cherry, Phys. Med. Biol. 54 (2009) 1291 (Mar).
[10] T. Hirai, R. Nohara, R. Hosokawa, M. Tanaka, H. Inada, Y. Fujibayashi, et al., J. Nucl. Cardiol. 7 (2000) 107 (3).
[11] C.-H. Hsu, P.-C. Huang, Comput. Med. Imaging Graph. 30 (2006) 181 (4).
[12] Y.-J. Qi, Nucl. Sci. Tech. 17 (2006) 164 (6).
[13] J. Nuyts, K. Vunckx, M. Defrise, C. Vanhove, Methods 48 (2009) 83 (6).
[14] H. Hsieh, I. Hsiao, Tsinghua Sci. Technol. 15 (2010) 44 (2).
[15] B. Jun Min, Y. Choi, N.-Y. Lee, J. Ho Jung, K. Jo Hong, J. Kang, et al., Nucl. Instrum. Methods Phys. Res., Sect. A 633 (2011) 61 (3).
[16] A. Del Guerra, C. Damiani, G. Di Domenico, A. Motta, M. Giganti, R. Marchesini, et al., IEEE Trans. Nucl. Sci. NS47 (2000) 1537 (Aug).
[17] C. Damiani, G. Di Domenico, E. Moretti, N. Sabba, G. Zavattini, A. Del Guerra, Sampling considerations for high resolution small animal SPECT, in: Nuclear Science Symposium Conference Record, 2002 IEEE, 2002, pp. 1770–1774.
[18] W. Choong, W.W. Moses, C.S. Tindall, P.N. Luke, Design for a high-resolution small-animal SPECT system using pixelated Si(Li) detectors for in vivo $<$sup$>$ 125 $<$/sup$>$I imaging, in: Nuclear Science Symposium Conference Record, 2003 IEEE, 2003, pp. 2315–2319 vol. 4.
[19] G.K. Loudos, K.S. Nikita, N.K. Uzunoglu, N.D. Giokaris, C.N. Papanicolas, S.C. Archimandritis, et al., Comput. Med. Imaging Graph. 27 (2003) 307.
[20] A.G. Weisenberger, J.S. Baba, B. Kross, S.S. Gleason, J. Goddard, S. Majewski, et al., Dual low profile detector heads for a restraint free small animal SPECT imaging system, in: Nuclear Science Symposium Conference Record, 2004 IEEE, 2004, pp. 2456–2460.
[21] S. Walrand, F. Jamar, J. Nucl. Med. 46 (2005) 1872.
[22] G. Loudos, S. Majewski, R. Wojcik, A. Weisenberger, N. Sakellios, K. Nikita, et al., Nucl. Instrum. Methods Phys. Res., Sect. A 571 (2007) 48.
[23] N. Sakellios, J.L. Rubio, N. Karakatsanis, G. Kontaxakis, G. Loudos, A. Santos, et al., GATE simulations for small animal SPECT/PET using voxelized phantoms and rotating-head detectors, in: Nuclear Science Symposium Conference Record, 2006. IEEE, 2006, pp. 2000–2003.
[24] G. Loudos, S. Majewski, R. Wojcik, A. Weisenberger, N. Sakellios, K. Nikita, et al., IEEE Trans. Nucl. Sci. NS 54 (2007) 454.
[25] E. Lage, J.J. Vaquero, J. Villena, A. de Carlos, G. Tapias, A. Sisniegaet al., Performance evaluation of a new gamma imager for small animal SPECT applications, in: Nuclear Science Symposium Conference Record, 2007. NSS '07. IEEE, 2007, pp. 3355–3360.
[26] J.L. Villena, E. Lage, A. de Carlos, G. Tapias, A. Sisniega, J.J. Vaquero, et al., A super-resolution feasibility study in small-animal SPECT imaging, in: Nuclear Science Symposium Conference Record, 2008. NSS '08. IEEE, 2008, pp. 4755–4759.
[27] H.O. Anger, Rev. Sci. Instrum. 29 (1958).
[28] S. Sajedi, A. Kamal Asl, M.R. Ay, M.H. Farahani, A. Rahmim, Med. Eng. Phys. 35 (2013) 754.
[29] R. Rojas, Kohenen's Model, in Neural Networks, ed, Springer-Verlag, Berlin, 1996.
[30] T. Kohenen, Self-Organization and Associative Memory, Springer-Verlag, Heidelberg, 1988.
[31] T. Kohenen, Self-Organization Maps: Optimization and Approaches, ICANN, Espoo, Finland, 1991.
[32] A.P. Dempster, N.M. Laird, D.B. Rdin, J. R. Stat. Soc. Ser. 39 (1977) 1.
[33] N. Zeraatkar, M.H. Farahani, H. Arabi, S. Sarkar, S. Sajedi, N. Naderi, et al., Eur. J. Nucl. Med. Mol. Imaging 39 (Suppl. 2) (2012) S386 (Abstract P210).

[34] B.F. Hutton, J. Nuyts, H. Zaidi, Iterative reconstruction methods, in: H. Zaidi (Ed.), Quantitative Analysis in Nuclear Medicine Imaging, Springer, Singapore, 2006.
[35] A. Rahmim, H. Zaidi, Nucl. Med. Commun. 29 (2008) 193 (Mar).
[36] E.C. Frey, B.M.W. Tsui, Quant. Anal. Nucl. Med. Imaging (2006).
[37] E.M. Geldenhuys, M.G. Lötter, P.C. Minnaar, J. Nucl. Med. 29 (1988) 538.
[38] H.O. Anger, Instrum. Nucl. Med. 1 (1967) 485.
[39] H. Jacobowitz, S.D. Metzler, Int. J. Math. Math. Sci. 2010 (2010).